JACS
JOURNAL OF THE AMERICAN CHEMICAL SOCIETY
Article
pubs.acs.org/JACS

Dynamics of Confined Reactive Water in Smectite Clay–Zeolite Composites

Michael C. Pitman*,† and Adri C. T. van Duin‡

†Soft Matter Theory and Simulations Group, Computational Biology Center, IBM Watson Research Center, Yorktown Heights, New York 10598, United States

‡Department of Mechanical and Nuclear Engineering, Pennsylvania State University, 136 Research East Building, University Park, Pennsylvania 16802, United States

ABSTRACT: The dynamics of water confined to mesoporous regions in minerals such as swelling clays and zeolites is fundamental to a wide range of resource management issues impacting many processes on a global scale, including radioactive waste containment, desalination, and enhanced oil recovery. Large-scale atomic models of freely diffusing multilayer smectite particles at low hydration confined in a silicalite cage are used to investigate water dynamics in the composite environment with the ReaxFF reactive force field over a temperature range of 300–647 K. The reactive capability of the force field enabled a range of relevant surface chemistry to emerge, including acid/base equilibria in the interlayer calcium hydrates and silanol formation on the edges of the clay and inner surface of the zeolite housing. After annealing, the resulting clay models exhibit both mono- and bilayer hydration structures. Clay surface hydration redistributed markedly and yielded to silicalite water loading. We find that the absolute rates and temperature dependence of water dynamics compare well to neutron scattering data and pulse field gradient measures from relevant samples of Ca-montmorillonite and silicalite, respectively. Within an atomistic, reactive context, our results distinguish water dynamics in the interlayer $Ca(OH)_2 \cdot nH_2O$ environment from water flowing over the clay surface, and from water diffusing within silicalite. We find that the diffusion of water when complexed to Ca hydrates is considerably slower than freely diffusing water over the clay surface, and the reduced mobility is well described by a difference in the Arrhenius pre-exponential factor rather than a change in activation energy.

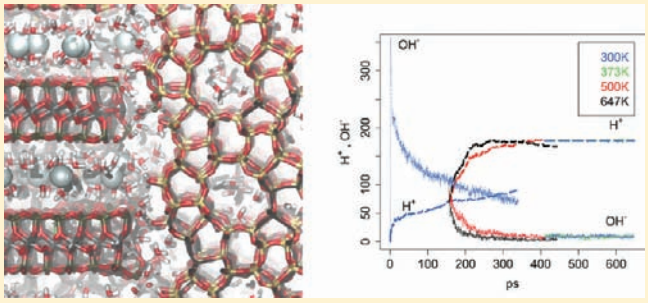

INTRODUCTION

Hydration and water dynamics in clay mineral environments intersect a broad range of interests, from the very fundamental questions of the origins of life[1,2] to the practical and important issues of resource management at scale.[3−9] Despite long-standing pursuit, fundamental questions about the mechanism of water dynamics and ion transport processes in clays have eluded a firm understanding.[10]

The microscopic details of confined water in clay environments present a host of challenges for simulation. The compositional variety and surface heterogeneities found in natural clays can demand a large minimal scale for an atomistic approach to ensure a representative variety. Clay surface chemistry is dynamic in many cases of interest, such as proton distribution along the edges of clay sheets. Despite difficulties, numerous simulation methods have been applied to clays and clay hydration, including bulk materials properties,[11,12] diffusion with various guest solutes,[13−15] and swelling.[16] Monte Carlo methods,[13,14,16] molecular dynamics (MD) methods,[11,12,15,17−19] and density functional methods[20,21] have been applied. Empirical force fields such as CLAYFF[19] have made substantial progress at characterizing clay properties.[11,12,17]

Hydration of smectite swelling clay systems is strongly impacted by both the mesoporous regions and the counterions.[7,8,22,23] As clay particles stack and interface with each other or with other mineral environments, mesoporous crevices form from nonideal packing.[22] The crevices and interlayers have distinct hydration properties and are greatly affected by the mineral environment and humidity levels. Addressing the relevant surface chemistry is a further challenge, as surface and edge modifications are intimately coupled to hydration and surface diffusivity, and the surface chemistry is dynamic on a time scale the same as or smaller than the time scale one is trying to characterize. In such cases, a fixed topology approximation underlying classical MD may limit the scope of applicability.

Accordingly, new physical insights may be gained as reactive atomistic models are scaled up to facilitate a relevant range of surface chemistry and interactions with water as it diffuses through porous cavities and interlayers of a mineral environment. An accurate characterization of water dynamics in mineral environments is needed for modeling flow in

Received: September 21, 2011
Published: January 10, 2012

   dx.doi.org/10.1021/ja208894m | J. Am. Chem. Soc. 2012, 134, 3042–3053

heterogeneous clay environments under spontaneous or driven conditions.

A goal of the present work is to assess water diffusion and dynamics as revealed in large-scale simulations of a clay−zeolite composite environment with a fully atomistic reactive force field. The present approach is intended to generalize to a broader range of solutes in clay mineral environments under a variety of nonequilibrium conditions.

A utility of reactive force fields is that diffusion-controlled reactions can and do occur at diffusive rates. While this can complicate some analyses, it can simplify some aspects of simulation design. Deterministically arranging an elemental composition for study, and relying on reaction−diffusion processes to locally arrive at chemical equilibrium, offers a more general capability relative to a corresponding classical force field where system topology remains constant throughout the simulation. During the diffusive processes, reactions and surface reforming continue, and the resulting rates reflect the compositional changes due to reactions, diffusion of reactants and products, and the coupling between compositional changes and the consequent effects on diffusivity.

A main function of the zeolite is to provide a periodic silicalite matrix that hosts the clay particle. The zeolite housing provides high-mobility paths for small-molecule transport under dynamic local pressure and chemical potential gradients. Overall temperature and pressure were regulated methodologically with a thermostat and barostat (NPT ensemble). However, the zeolite matrix ensures that the dominant mechanisms of local pressure and chemical potential equilibration were consistent through explicit atomistic transport modes within the simulation (i.e., redistribution and reaction with water). Here, the zeolite will serve as an independently characterizable, porous yet confining reference environment to facilitate direct comparison of clay particles from different simulations. We should emphasize, though, that in addition to methodological limitations to ReaxFF, the conditions imposed by the zeolite housing at a particular solvent and solute loading represent a highly specific environment to which the clay particle must adapt, and that may limit the scope of what natural mineral compositions the models could inform.

We performed MD simulations using the ReaxFF reactive force field method.[24] This method allows us to model moderately large systems efficiently while still retaining near quantum mechanical accuracy, especially for reaction barriers and reaction energies.[25] ReaxFF combines a bond-order concept[26−29] with a polarizable charge model,[30] which enables the method to model the breaking and formation of bonds and the associated charge rearrangements during an energy-conserving MD simulation.

We present a reactive force field based approach effective for studying clay−zeolite composite systems. Targeting Ca-montmorillonite as the representative swelling clay, we constructed a series of large-scale clay−zeolite systems through a combination of algorithmic and preparative reactive simulations, as illustrated in Figure 1. We report structural and dynamic results for the compositions including basal spacing, Ca cluster size distribution, and regional-specific transport and reorientational dynamics for water and Ca-$(OH)_2$·nH_2O through the confined interstitial crevices of the model clay−zeolite composites. We show that our reactive protocol yields acid/base equilibrium product distributions of $[H^+](t)$ and $[HO^-](t)$ and silanol formation in clay and zeolite models. We find that the present method yields accurate diffusion and reorientational dynamics for water in the represented environments, which compare well to available experimental measures.

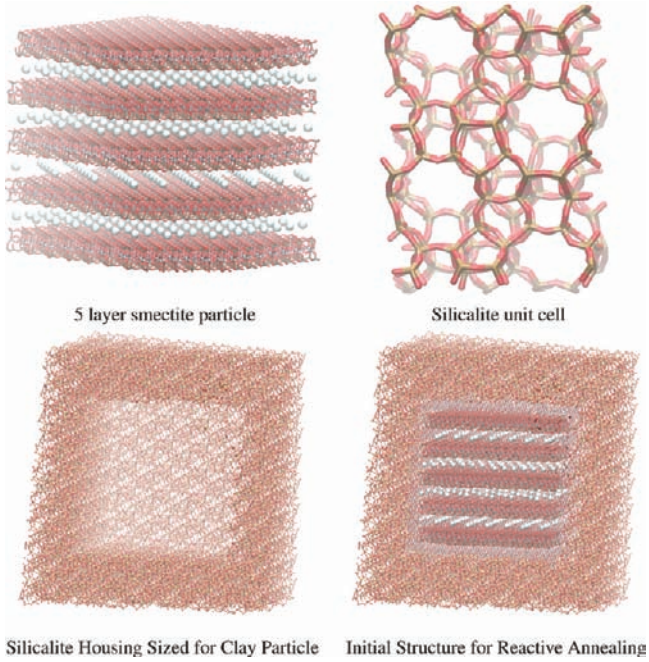

Figure 1. Stages of construction for clay−zeolite composite system. (Top left) A five-layer particle constructed from 11 × 9 × 5 unit cells of smectite,[31] where each clay stack is rotated 60°. (Top right) Unit cell of the all-silicaceous zeolite ZSM5-silicalite. (Bottom left) Silicalite unit cells are stacked in a shell to create a housing that can accommodate the clay particle with room for a thin layer of water across the clay−zeolite interface. (Bottom right) The trimmed clay particle placed in the silicalite housing with water placed on a lattice throughout the clay calcium interlayer and clay−silicalite interface.

METHODS

Clay Composition and Layer Charge. The basic smectite sheet has the pyrophyllite structural unit $Si_8O_{20}(OH)_4$, in a 2:1 arrangement of tetrahedral silicate and octahedral aluminum layers. In natural clay minerals, isomorphic substitution of Mg or Fe for Al in the octahedral layer (montmorillonite) or for Si in the tetrahedral layer (beidellite) gives rise to a permanant charge in the clay layer. Swelling clays have a distinct range of layer charge that enables humidity-dependent hydration of the interlayer. Layer charge in montmorillonites can range between −0.6 and −1.2 per $Si_8O_{20}(OH)_4$. Substitutions that give a larger permanent layer charge are found in micas, with a permanent charge of −2 per $Si_8O_{20}(OH)_4$. Mica sheets accommodate counterions in the interlayer, but do not swell with changes in humidity.

In ReaxFF, the charge carried by an atom is a dynamic quantity, not presently subject to explicit constraints. This removes the option of fixing a particular layer charge. To characterize how composition impacts layer charge, we prepared a series of smectite clay compositions that represent a range of formal charge states from −4 per $Si_8O_{20}(OH)_4$ to neutral. The neutral clay was simulated with and without the presence of calcium salts. Table 1 details the compositions used in this study.

We modeled the layer charge effects of Mg for Al substitutions in the octahedral layer by varying the protonation state of the clay lattice hydroxyl groups, rather than explicit introduction of Mg, for two reasons. First, Mg parameters were not available. Second, this is reasonable provided it can be verified that the lattice hydroxyl hydrogens are chemically isolated in simulation and do not directly participate in acid/base equilibria (which we show is the case here). Provided the clay lattice structure is unperturbed by varying the

dx.doi.org/10.1021/ja208894m | J. Am. Chem. Soc. 2012, 134, 3042−3053

Table 1. Model Clay Composition Series[a]

label	model clay structure formula	counterion	formal q per Si_8	isoelectronic Mg isomorph
LH0	$Al_4Si_8O_{24}$	(H)(Ca)	−4	$Mg_4Si_8O_{20}(OH)_4$
LH2	$Al_4Si_8O_{22}(OH)_2$	Ca	−2	$Mg_2Al_2Si_8O_{20}(OH)_4$
LH3	$Al_4Si_8O_{21}(OH)_3$	CaOH	−1	$MgAl_3Si_8O_{20}(OH)_4$
LH4	$Al_4Si_8O_{20}(OH)_4$	$Ca(OH)_2$	0	
LH4W	$Al_4Si_8O_{20}(OH)_4$	(H)(OH)	0	

[a]Each label indicates a clay composition, counterion, and formal layer charge per structure unit that was simulated in a zeolite housing.

protonation levels of the lattice hydroxyls, and the environment of the clay does not directly contact the octahedral layer, we may consider $Al_4Si_8O_{21}(OH)_3$ a model of $MgAl_3Si_8O_{20}(OH)_4$ for purposes of assessing layer charge effects.

Table 1 shows the series of compositions, the formal charge per Si_8 structure unit, the counterion species available for balance, and the corresponding Mg substitution pattern of the same formal charge. Of these, LH3 most closely represents a smectite clay. LH4 and LH4W represent pyrophyllite with and without Ca salts present in the interlayer. LH2 and LH0 represent compositions of micas.

Smectite Clay Particle Preparation. Targeting Ca-montmorillonite as the representative swelling clay, we constructed a series of large-scale clay−zeolite systems through a combination of algorithmic and preparative reactive simulation, as illustrated in Figure 1. Each of the clay particles is prepared with five stacked and rotationally disordered smectite layers and Ca as counterions in the interlayer. Table 1 summarizes the compositions studied.

We prepared smectite particles by stacking smectite layers built up from unit cells of crystallographic coordinates.[31] The intention was to determine the initial clay and counterion configurations, solvate the system with water, and allow protonation and hydroxylation reactions to equilibrate as we monitor convergence of pH. The counterions and the lattice hydroxyl hydrogens (LHHs) were added according to the compositions in Table 1. The unit cell structure presents two possible Ca sites with 50% occupancy. Ca was placed at every other site for all compositions expect for LH4W (which contained only water and neutral clay). LHHs were added according to the composition scheme shown in Table 1. For LH3, an explicit CaOH was placed in the interlayer parallel to the clay sheets, with the Ca occupying a counterion position from the unit cell.

The clay particles were made from 11 × 9 × 5 unit cells using lattice parameters a = 5.18, b = 8.98, and c = 15.0 Å. The stacking transformation in the orthogonal coordinate system compensates the monoclinic distortion by adding $s^0 = \{-0.5628a,0,c\}$ to a sliding translation of $s^{xy} = \{a/3,b/3,0\}$. The resulting stacking vector s_i for layer index i is $s_i = i(s^0 + s^{xy})$, where i is the layer number. Each layer was rotated through a spiral sequence by 60° according to $\theta_i^z = (\pi/3)i$, which has the desirable effect of lowering the symmetry of the clay and allowing the simulation to sample a broader range of hydration interactions. As the layers are stacked and rotated, Ca atoms are placed in the corresponding sites for the composition and unit cell, until the final stack, which caps the clay particle. This protocol deterministically produces clay structures that are suitable for simulation with ReaxFF for equillibration of pH. The initial clay structure has exposed edges and unsolvated Ca salts between the clay sheets. We intentionally leave these aspects of the system open and leverage the reactive force field for finishing reactions on the surfaces. Figure 1 illustrates the construction of clay−zeolite composite systems. The system parameters used for the present work are summarized in Tables 2 and 3.

Zeolite Housing Preparation. We chose zeolite ZSM-5 to provide a boundary material suitable for use as a periodic matrix that will house the clay particle. ZSM-5 has a chemical formula of $Na_nAl_nSi_{96-n}O_{192}\cdot 16H_2O$ ($0 < n < 27$). We further chose the dry, all-silicaceous form silicalite, where n = 0, giving the unit cell a formula of $Si_{96}O_{192}$.

Table 2. Composition Series System Parameters

	LH0	LH2	LH3	LH4	LH4W
total atoms	97 948	98 651	96 388	99 284	103 268
initial waters	6326	6319	5251	6298	7723
Ca atoms	287	287	287	287	0

Table 3. Zeolite Housing and Particle Shaping Parameters

silicalite lattice constants (Å)	{20.11,19.88,26.74}
silicalite N unit cells	5 × 6 × 5
initial silicalite formula	$Si_{21888}O_{43686}$
clay lattice constants (Å)	{5.18,8.98,15.0}
clay layer N unit cells	11 × 9 × 5
bond order threshold, Θ_{min}	0.4
clay−zeolite interface (Å)	6.5

The housing for the clay particle was constructed by configuring a zeolite shell, one unit cell thick on all sides.The periodic boundary cuts cleanly along each face of the zeolite unit cell group. The zeolite unit cells along the faces of the full system boundary (as opposed to the edges or corners) touch the periodic boundary on one face and the housing on the opposing face. This allows exposure and derivitization of the opposing surface as the housing wall. The guest particle is presented independent, porous walls in every direction that reactively adjust to the specific guest environment.

The explicit boundary approach taken here requires much of the system to implement the boundaries. A five-layer smectite particle of near cubic shape housed with a one unit cell thick zeolite boundary spends three-quarters of the system atoms implementing the zeolite environment. Having one unit thick walls on all sides provides two unit cells in each direction for transport and buffering capacity between periodic images, and also provides a reference environment for the clay that is comparable to experiment over a range of clays. Since the clay stacks were rotated and shifted, the fit is generally rough and overlapping. A parameter that defines the desired thickness of the interstitial layer across the clay−zeolite interface, Δ_I, is used to remove clay atoms that are within Δ_I from the inner zeolite housing surface. To ensure the clay extends to at least Δ_I from the wall, extra clay unit cells are added to each stack during the clay particle construction. The application of Δ_I carves the clay particle to fit within the zeolite housing and ensures a minimum spacing for solvent. The resulting fit gives an unfinished surface to the edges of the clay stacks. For the present work, we used Δ_I = 6.5 Å.

The system is solvated after the clay particle is placed within the zeolite housing and carved to fit with a Δ_I thick clay−zeolite interface. Solvation of the system proceeds, where space permits, by placing water systematically on a cubic lattice with spacing to place the water O atoms 2.8 Å apart, which begins the simulation with the waters in H-bonding range. Waters are placed only on lattice points where the closest pre-existing atom is more than an empircial 3 Å away. The interstitial layers between the clay sheets and the clay−zeolite interface are solvated with an initial water count shown in Table 2. This leaves the water loading low, corresponding to low humidity levels, and creates a system where several simultaneous reactions involving water progress toward an equilibrium distribution. The final equilibrium distribution of H will partition across not only water locality (clay, zeolite, interface) but also the reaction products of water with the interlayer $Ca(OH)_2\cdot nH_2O$, the SiOH on the surface of the clay and zeolite, and acid/base equilibria throughout the system.

Reactive Simulations. The Reax/c implementation[25] in LAMMPS[32] was used for all simulations in this work. All runs were carried out in the NPT ensemble at 1 atm pressure, with a time step of 0.25 fs. Systems were run on 512 and 1024 nodes of Blue Gene/L at IBM Watson Research Center Supercomputing Facility.

The O/H ReaxFF parameters used in this study were trained against a substantial DFT-based training set containing, among others, water binding energy for clusters containing 2−35 water molecules, bond dissociation energies in H_2O, O_2, and H_2, concerted proton-

dx.doi.org/10.1021/ja208894m | J. Am. Chem. Soc. 2012, 134, 3042−3053

transfer barriers in $[H_2O]_x$ clusters (x = 2−6), proton-transfer reactions in OH^-/H_2O and H_3O^+/H_2O clusters, H−O−H and H−O−OH angular distortions, H_2O monomer and dimer vibrational frequencies, and equations of state for various ice crystals. These O/H parameters have been previously used to study a number of water/oxide interfaces, including water/ZnO,[33,34] water/FeO_x,[35] water/SiO_2,[36] water/CuO_x,[37] and water/Al-metal surfaces. For this study, we combined the previously reported H/O/Si[36] and H/O/Al[38] ReaxFF descriptions and added to this parameter set a recently developed set of ReaxFF parameters for Ca/O and Ca/H interactions.[39] These Ca/O/H parameters were derived against a DFT-based training set describing Ca^{2+} and $CaOH^+$ ion solvation in water, Ca-metal, and CaO-crystal formation energies, energy/volume relation, surface energies, and water binding energies to CaO surfaces. For a more elaborate description of the ReaxFF method, please refer to the recent review by Russo et al.[40] and references therein.

Analysis of Confined Water. Water was analyzed by diffusion and reorientational correlation times in particular regions of interest. Two regions, the zeolite matrix and the housing region, are defined geometrically such that together they span the full simulation cell and have no overlap. The zeolite matrix is defined as the region containing a shell around the cell boundaries with a thickness of one unit cell in from the simulation cell boundary. This region contains all zeolite structure, including its channels. Its counterpart is the housing region, which contains the clay particle and all solvent not in the zeolite region.

Diffusion and reorientational rates are then calculated for each region. Diffusion coefficients are commonly evaluated from the mean-squared displacement of a diffusing body with time as $\langle \Delta r(t)^2 \rangle = 2dDt$, where brackets denote ensemble average, $\Delta r(t)$ is the displacement after time lag t, D is the diffusion coefficient, and d is the dimensionality of the corresponding displacement metric $\Delta r(t)$. Estimates of diffusivity in confined or inhomogeneous fluids must take into account the confining geometry and the time particles spend in particular regions. The method proposed by Liu and Berne[41] was adapted to the present regional scheme for the calculation of diffusion coefficients within each region. A survival probability $P(t)$ for a region enters into the mean squared displacement relation as $\langle \Delta r^2 \rangle = 6DP(t)t$. The decay of the population in the region of interest is calculated as

$$P(t) = \frac{1}{T}\sum_{t}^{T} \frac{N(t,\tau)}{N(t)}$$

where $N(t,\tau)$ is the probability of a particle at time t surviving the inclusion criteria for a duration of τ, $N(t)$ is the number of members contributing to the class at time t, and T is the number of time steps contributing to $P(t)$.

For processes undergoing simultaneous reactions during diffusion, measures of population displacement in a region will include changes in the diffusing population due to reaction kinetics. Reactive mechanisms will affect the production and decay of a species in a region, and this will have an effect on the resulting ensemble averages of displacement for the species in the region. A straightforward adaptation of the regional survival probability in reactive systems is to further qualify the time-dependent concentration $N(t)$ to include both geometric and topological qualification to the survival probability $P(t)$. The effective dimensionality of diffusion is treated as three-dimensional and isotropic, due to the variety of confining geometries present.

Reorientation rates are calculated from the relaxation time of the correlation function $C(t) = \langle P_2[\mu_{OH}(0)\mu_{OH}(t)] \rangle$, where P_2 is the second-order Legendre polynomial and $\mu_{OH}(t)$ is the orientation of the OH bond at time t. The decay of the reorientational correlation function P_2 was modeled with a stretched exponential.[42] Thus, $C(t) = A\exp(-t/\tau c)^{\beta}$, where τ_c is the characteristic decay time and β is the stretching exponent. Lower values of β give a broader distribution of lifetimes, corresponding to a wide range of environments. The average lifetime is related to the characteristic lifetime through

$$\langle \tau \rangle = \frac{\tau_c}{\beta}\Gamma\left(\frac{1}{\beta}\right)$$

where $\Gamma(x)$ is the gamma function.

Analysis of Bonding and Reactions. When analyzing reactive trajectories, determining which species are present at any given time, and in what numbers, involves a somewhat arbitrary choice of cutoff in bond order, Θ_{min}, which defines the minimum bond order to be considered covalent. Bond orders greater than this value at time t are considered covalent over the time interval $(t,t+\Delta t]$ and will determine the molecular species present at that time interval. The threshold is influenced by temperature and other simulation conditions. As Θ_{min} is lowered, more extended complexes emerge as a result of less restrictive instantaneous geometrical relationships qualifying as covalent bonds. When weaker bonds are classified as covalent, larger and more complex molecules are identified from the more extended bonding networks. Upper bounds can be found empirically by examining whether the instantaneous concentrations of $[H_3O^+]_t$ and $[H^+]_t$ are reasonable. For example, if we compute $[H^+](t)$ from $([H^+]_t + [H_3O^+]_t)/[H_2O]_t$, we find that ensemble average $\langle [H^+]_t \rangle \rightarrow 0$ for $\Theta_{min} \leq 0.5$, and acidity is carried through the $[H_3O^+]$ component as $[H^+](t) \approx [H_3O^+]_t$.

After considering the effects of varying Θ_{min} on the time-dependent species count (molecule concentration), we set Θ_{min} = 0.4 for the initial bond assignments from the trajectory. The full distribution of molecules present at time t is given by enumeration of the isolated subgraphs, given the covalent bond assignments occurring at time t. The molecule distribution over each trajectory is tabulated and used to estimate the time-dependent concentration for the species of interest over time.

Assessing $[Ca^{2+}](t)$ and $[Ca(OH)^+](t)$ is more complex due to the extended $[Ca(OH)_2{\cdot}nH_2O]$ structures that form dynamically over the course of the simulation. From the full system molecule assignments under a given Θ_{min}, all molecules containing Ca are tabulated according to Ca count within the instant molecule. The distribution of cluster sizes is determined from an appropriate time average. For the composition series, the final 40 ps of the post-annealed trajectory is used for Ca cluster statistics.

Calculation of pH. For the present work, we focused on water with corresponding acid/base equilibria and water in Ca hydrates. A definition of a species concentration that is less sensitive to the arbitrary bond threshold than the raw count of the species is as follows. We define $[X]_t$ as the raw count of the species in the system as identified by Θ_{min} at time t, and $[X](t)$ as the effective concentration at time t used for analysis. $[H_2O](t)$ can be estimated directly from $[H_2O]_t$. However, we find that the OH^- forms a complex with water wherever $OH^-\cdots OH_2$ interactions have sufficiently high bond orders to exceed Θ_{min}. When these occur with sufficient strength, they are classified as covalent, though we would rather consider them as complexed. We treat this case by tracking $[H_3O_2^-]_t$ over the trajectory and include an additional water and hydroxide ion for each water−hydroxide complex present: $[HO^-](t) = ([OH^-]_t + [H_3O_2^-]_t)/([H_2O]_t$. Correspondingly, H_3O^+ can complex with water, where the bridging $OH_2H^+\cdots OH_2$ has a bond order greater than Θ_{min} and is identified as $[H_5O_2^+](t)$, and $[H^+](t) = ([H^+]_t + [H_3O^+]_t) + [H_5O_2^+]t)/([H_2O]_t)$. Our estimate for the instantaneous concentration of water is $[H_2O](t) = [H_2O]_t + [H_3O_2^-]_t + [H_5O_2^+]_t$. These expressions were used to estimate pH and related species shown in Figure 6 (below).

RESULTS

Relaxation of the clay particles in the zeolite housing with a reactive force field allowed several reactions to proceed prior to any substantial diffusion. Unfinished clay and zeolite surfaces exposed during the setup protocol react with water in the immediate vicinity to form silanol through both $O_nSi{-}O^-$ +

$H_2O \rightarrow O_nSi{-}OH + OH^-$ and $O_nSi^+ + H_2O \rightarrow O_nSi{-}OH + H^+$ pathways. The initial silanol surface reactions occur on the clay and zeolite surfaces. Surface modifications continued to reform the surface over the course of the annealing cycle. Calcium and water rapidly formed lime hydrates as $Ca + H_2O \rightarrow Ca(OH)_2{\cdot}nH_2O$.

Examination of the post-annealed smectite structures showed that the initial LHH configuration was stable to the annealing protocol. That is, the initial LHH pattern was still present. The LHH did not exchange with the solvent in LH4 or LH4W, nor were there cases of protonation of vacant LHH sites from solvent in LH0, LH2, or LH3.

Figure 2 shows the distribution of basal spacings, *d*, for the post-annealed clay series. For compositions where Ca was

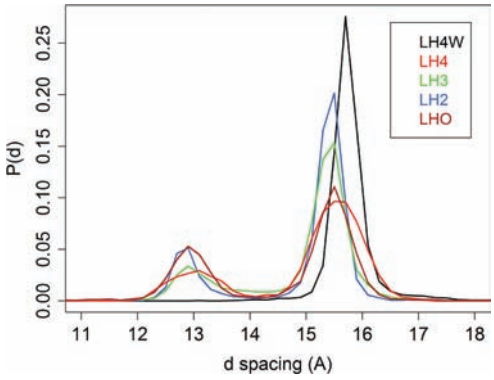

Figure 2. Comparison of resulting basal spacing *d* for the post-annealed particles in the composition series. For the five clay layers present, a histogram of the Al–Al interlayer height difference for adjacent layers is shown in the single-layer range. The model pyrophyllite composition exhibits bilayer hydration only. All other compositions formed a mixture of mono- and bilayer hydration levels.

present, all but one of the four interlayers formed a monolayer hydration pattern. Bilayer hydration resulted in three of the four interlayers in all but LH4W, which exhibited bilayer hydration throughout.

Figure 3 shows the distribution of Ca cluster sizes. The structural variation of the calcium interlayer is quite complex

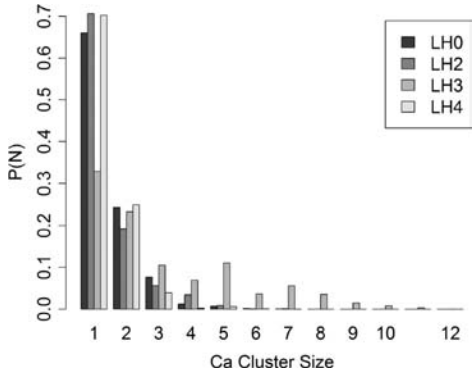

Figure 3. Ca cluster size distribution for composition series. A complex distribution of $Ca(OH)_2{\cdot}nH_2O$ clusters emerges consistently across the compositions. With composition LH3, we see larger clusters precipitate. All other Ca compositions investigated formed clusters of less than four Ca per cluster (see text).

across the series. We see a similar distribution of cluster sizes with the exception of LH3, which had the Ca species initially arranged as CaOH. Here the OH group occupies space that would have been occupied by H_2O, as in the other compositions. The substantial reduction in H/O ratio resulted in precipitation of $Ca(OH)_2$.

Figure 4 shows the diffusivity for water at 300 K across the composition series, in comparison to experimental data from

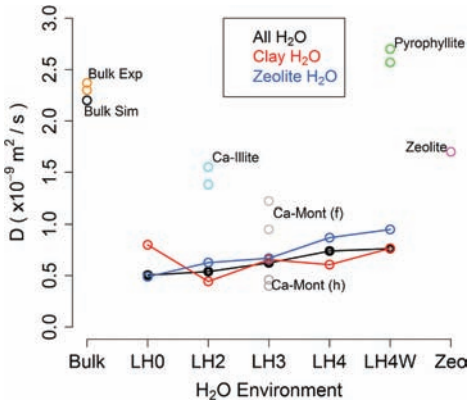

Figure 4. Water diffusivity for the post-annealed composition series compared to QENS data from Sánchez[43] at 300 K. Three classes of diffusivity are shown. Diffusivity of all water in the system is shown as the black points and lines. The blue series is specific to water in the zeolite region. The red series is specific to water in the clay region. Lines are shown as a visual aid. QENS data (at 298 K) for various minerals are shown as labeled pairs of open circles, positioned over the closest compositional analogue in the series. Each pair corresponds to the two analysis models applied to the QENS data. The QENS value for bulk water diffusivity is shown for reference and is compared to the bulk diffusivity calculated with the present ReaxFF parameters used for this work. The zeolite value in magenta is from ref 44.

ref 43. Calculated diffusivities for H_2O in the clay and zeolite regions for each composition are shown as combined lines and circles. The compositions are arranged in order of increasing LHH count. Water in bulk and in zeolite are shown on the left and right, respectively. Diffusivity for all H_2O in the post-annealed simulation is shown in black. H_2O found only in the zeolite or clay region is shown in blue or red, respectively. Experimental values for bulk water and in a zeolite at 300 K are included for comparison. Diffusivity for samples of Ca-montmorillonite[43] in full (bilayer) and half (monolayer) hydration levels are shown in gray, Ca-illite in cyan, pyrophylite in green, and bulk water in orange. The experimental data from ref 43 are shown as pairs of open circles, with each pair corresponding to the values for both quasi-elastic neutron scattering (QENS) analysis models. The range of calculated diffusivities lies within the two experimental hydration levels for Ca-montmorillonite at 300 K. Our calculated bulk value is 2.2×10^{-9} m^{-2}/s, which is shown compared to the experimental bulk value detemined in the QENS analaysis.[43]

Reactions of Water. In the LH0 composition, all of the hydrogen in the system originates from $[H_2O]_0 = 6326$ water molecules. Figures 5 and 6 show $[H^+](t)$ and $[HO^-](t)$ from the initial structure through a first annealing cycle. The color of the series corresponds to the temperature at which the simulation was run, with the *x*-axis indicating simulation time from the initial structure. A structure near the 150 ps mark was taken as the starting point for a temperature series $T = \{273,300,350,373,400,500,647\}$ K. The inset graph shows a closer view of $[H_2O](t)$ at selected temperatures. The series at

dx.doi.org/10.1021/ja208894m | J. Am. Chem. Soc. 2012, 134, 3042–3053

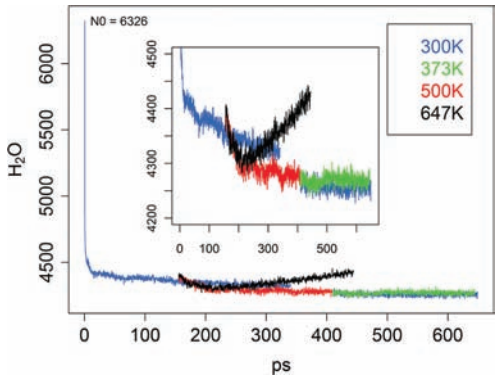

Figure 5. $[H_2O](t)$ during sample annealing. The color of the series corresponds to the temperature at which the simulation was run, with the *x*-axis indicating simulation time from the initial structure. A structure near the 150 ps mark was taken as the starting point for a temperature series T = {273,300,350,373,400,500,647} K (selected temperatures are shown for clarity). The inset graph shows a closer view of $[H_2O](t)$ at selected temperatures. The series at 500 K is shown in red, which continues for an additional 200 ps. The final structure from the T = 500 K series was used as the beginning of two additional trajectories at T = {300,373} K. The final, post-annealed structure at T = 300 K is shown in Figure 7.

500 K is shown in red, which continues for about 200 ps. The final structure from the 500 K series was then used as the beginning of two additional runs at T = {300,373} K. The final, post-annealed structure at T = 300 K is shown in Figure 7. The continuation of the 300 K series after selection of the starting structure for the temperature series (blue series from 150 to 350 ps) shows that $[H_2O](t)$ continues to drop at the same rate. $[H_2O](t)$ drops much faster at higher temperatures. Particular to the series near water's critical point (T = 647 K), $[H_2O](t)$ begins to increase. All lower temperatures investigated followed the trend exhibited by the 500 K series, but at slower rates. Figure 6 shows $[HO^-](t)$ increase followed by a subsequent, slower decay. The increase in $[HO^-](t)$ gives a pH value in agreement with saturated solutions of lime, which have pH = 12.4. The Ca hydrates form extensive, dynamic networks. The $[H^+]$ increases at a slower rate, and the two concentrations cross after 300 ps at T = 300 K. The rate increases at the annealling temperature and reaches limiting values within 250 ps at 500 K. The post-annealed simulations at 300 and 373 K show stable concentrations of $[H^+](t)$ and $[HO^-](t)$, indicating steady-state conditions for pH.

Diffusion of Water through the Clay–Zeolite Matrix. Figure 8 shows the region-specific Arrhenius plots for water displacement through the system. The displacement curves in Figure 8, top, show $\langle \Delta r(\tau)^2/P(\tau)\rangle$, which is the mean-squared displacements corrected for the survival probability for the region, $P(\tau)$, according to the method of Liu and Berne[41] and adapted here to include reactive decay pathways. The region shown is specific to water surrounding the clay particle, within the zeolite housing. The temperature dependence of the resulting (3D isotropic) diffusion coefficients for water is shown in Figure 8, bottom. Water within the zeolite matrix is shown in green. Water in the clay housing (corresponding to the displacement curves above) is shown in blue. Water or OH groups that are complexed with calcium are shown in red. QENS data from Sánchez et al.[43] and pulse field gradient (PFG) NMR data from Bussai et al.[44] are included for comparison. Bulk water is shown in brown. Two different fit

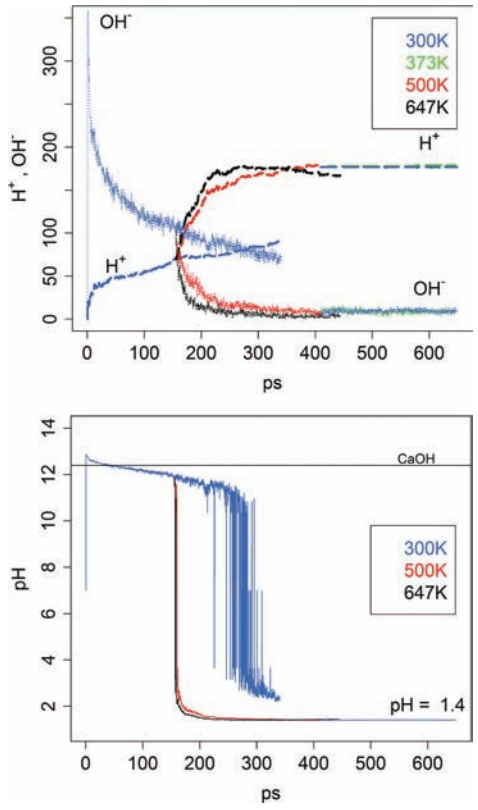

Figure 6. pH versus time. (Top) $[H^+](t)$ and $[HO^-](t)$ throughout the annealing cycle. Initially, $[HO^-](t)$ rises sharply to a maximum value and then decays more slowly. $[H^+]$ increases at a slower rate, and the two concentrations cross after 300 ps at T = 300 K. This rate is much faster at the annealing temperature and reaches limiting values within 250 ps at 500 K. The post-annealed simulations at 300 and 373 K show steady concentrations of $[H^+](t)$ and $[HO^-](t)$, indicating steady-state conditions for pH. (Bottom) pH of the pre- and post-annealed systems vs time. The pH of the 300 K system transitions to acidic around 300 ps. The high-temperature runs transition at an accelerated rate and converge with pH = 1.4. The final pH showed no temperature sensitivity from the post-annealed runs at 300 and 373 K.

models applied to QENS measurements of compacted, fully hydrated Ca-montmorillonite particles are shown in black and gray dashed lines. Half-hydrated samples from the same QENS study are shown in black and gray open circles.[43] Solid lines are fits to data from this work, and dashed lines are fits to the experimental data. The corresponding region-specific diffusion coefficients are given in Table 4, and diffusion Arrhenius parameters are given in the Figure 8 legend (in kcal/mol) and summarized in Table 5.

Regional Reorientation Dynamics for Water and CaOH. Figure 9, top, shows the stretched exponential fits to the reorientational correlation functions for OH groups in water throughout the clay region. Figure 9, bottom, shows Arrhenius data for reorientational time versus temperature specifically for water in zeolite and clay regions. Within the clay region, we show that OH bound in Ca clusters separately from water. The activation energies for reorientation are summarized in Table 7 and in the legend of Figure 9, bottom. The best-fit lines through the Arrhenius data in Figure 9, bottom, are shown for water in zeolite (blue), water in the clay region (green), and OH bound to Ca clusters (red). For comparison, the QENS data[43] are included, as was done with the diffusivity in Figure 8. The QENS rotational relaxation times for water in fully

dx.doi.org/10.1021/ja208894m | J. Am. Chem. Soc. 2012, 134, 3042–3053

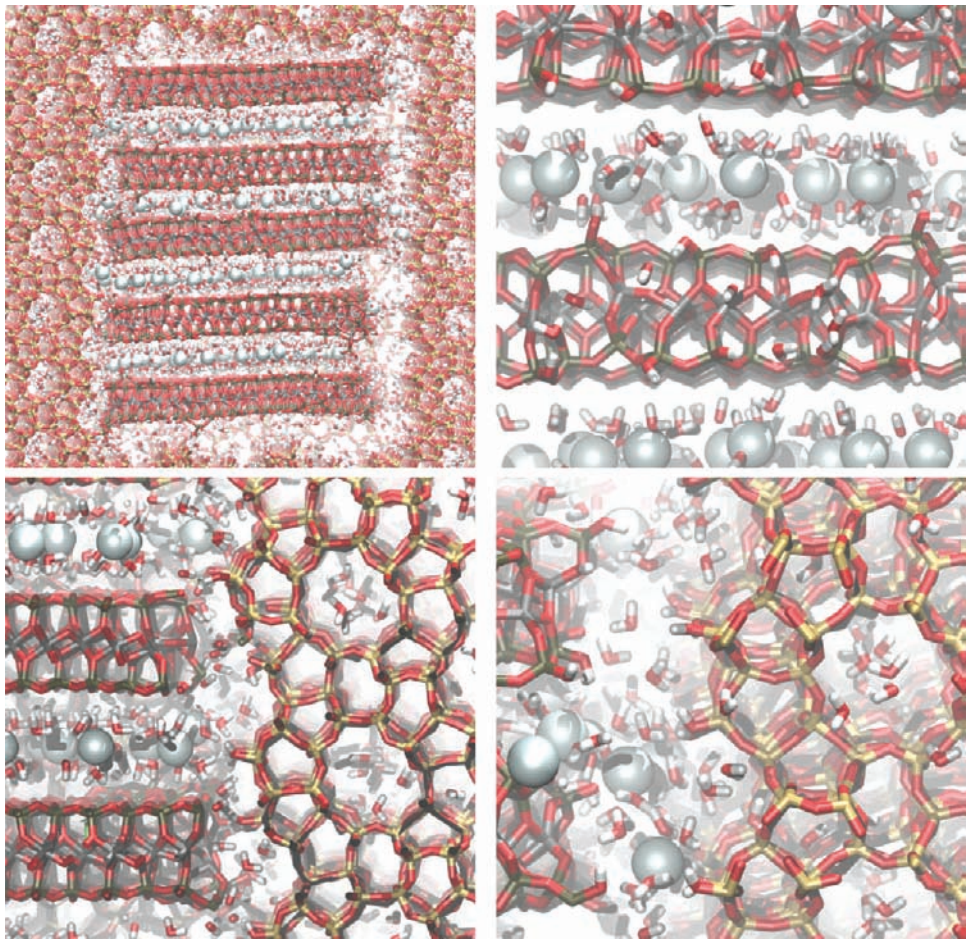

Figure 7. Selected views of the clay particle in silicalite housing after annealing at T = 500 K and re-equilibration at T = 300 K. Color scheme: aluminum, gray; clay silicon, dark green; zeolite silicon, tan; oxygen, red; hydrogen, white; calcium, light spheres. (Top left) View of full particle. The water is distributed with fairly uniform density within the zeolite matrix but exhibits some regional dewetting along the clay−zeolite interface, which is shown in the lower and right faces of the clay particle in the figure. The skew of the clay sheets is apparent and consistent with the monoclinic distortion found in the crystal structure. (Top right) View of calcium interlayer with bilayer hydration. Also visible are silianols on the clay sheet surface. (Bottom left) Surface of clay (left) interacting with silicalite (right). (Bottom right) Exchangeable calcium ions which have diffused into the clay−zeolite interface after being expelled from the calcium interlayer during a transition from bilayer to monolayer hydration.

hydrated samples (black) are fairly unaffected relative to bulk water measured (brown) with the same technique.[43] We find larger differences between the calculated values, longer relaxation times, and a larger rotational activation energy.

■ DISCUSSION

The initial system construction placed water throughout the clay region, intentionally leaving much of the zeolite dry (see Figure 1, bottom right, and Table 2). By geometrically connecting the water layer to both the interstitial calcium and the zeolite matrix, a balanced chemical potential for water μ_{H_2O} must balance relative forces of zeolite water loading with clay surface hydration, clay interstitial layer hydration, and $Ca(OH)_2{\cdot}nH_2O$ equilibria. The tendency for silicalite to absorb moisture is greater than hydration of the clay particle surface, but not the interlayer hydration. The water that remains in the calcium interlayers is clearly distinct from clay surface hydration. The clay interlayer hydration was stable to high temperatures, yet the clay surface water was partially dried by the zeolite. Water diffuses into the zeolite matrix from the clay housing at the expense of the interstitial crevices between the clay and the zeolite housing surface.

Figure 5 shows that as much as a third of the water was consumed in the first few picoseconds. Analysis of the dynamic system topology indicates this water is forming Ca hydrates and silanols. The complex distribution for Ca clusters shown in Figure 3 appears very early and evolves over the simulation. Figure 6 indicates that Ca hydrate formation drove the system to pH ≈ 12.4, in good agreement with the pH-saturated $Ca(OH)_2$ solution. Application of a thermal annealing cycle brought the system to a stable value of pH = 1.4 for LH0. The full series ranged from pH = 1.4 to 1.8, reflecting a net consumption of hydroxide due to surface reactions and hydrate formation. At the highest temperature investigated, T = 647 K (critical temperature for water), $[H_2O]$ began to increase at the expense of $[H^+]$, as seen in Figures 5 and 6 in both water increases and H^+ decreases (black series). This change was not observed at the lower temperatures and is attributed to dehydration of $Ca(OH)_2{\cdot}nH_2O$ in the interlayer in a strongly acidic environment at water's critical temperature.

The annealing cycle yielded an equilibrium partitioning of water across the clay−zeolite interface. The clay particles were stable to the high temperatures and relaxed in the housing as hydrated particles. As seen in Figure 7, top left, the particle sheared slightly and adhered to the housing walls through a thin

dx.doi.org/10.1021/ja208894m | J. Am. Chem. Soc. 2012, 134, 3042−3053

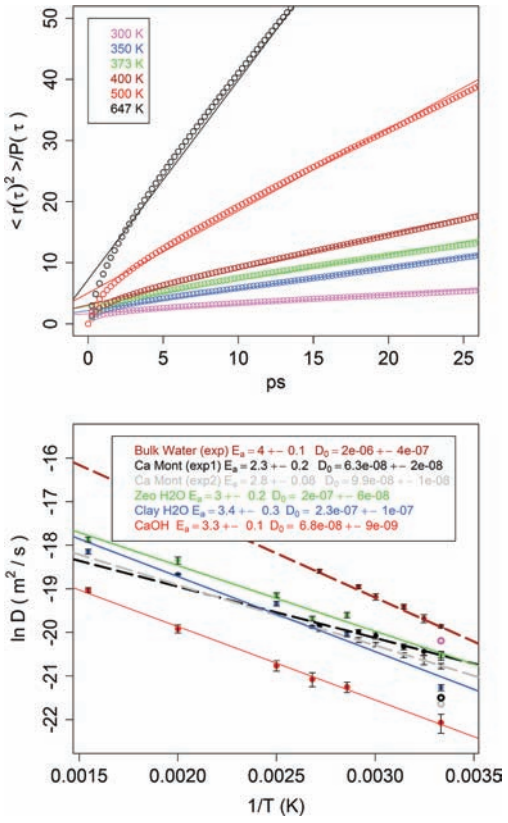

Figure 8. Diffusivity of water vs temperature. (Top) Displacement curves for water in the clay region normalized by survival probability.[41] (Bottom) Arrhenius plot for diffusion of water and calcium hydrate through the clay–zeolite matrix. Water in the zeolite matrix is shown in green. Water in the clay housing is shown in blue. Diffusion of HO groups bound to complexes is shown in red. QENS data[43] and PFG NMR measurements[44] are included as dashed lines and open circles for comparison (see text). Region-specific diffusion activation energies are given in the bottom figure legend (in kcal/mol) and summarized in Table 5.

Table 4. Region-Specific Diffusivity ($\times 10^{-9}$ m^2/s) of Water through the LH0 Model Clay and Silicalite

T (K)	$D^{all}_{H_2O}$	$D^{zeo}_{H_2O}$	$D^{clay}_{H_2O}$	D^{clay}_{CaOH}
300	0.72 ± 0.08	1.2 ± 0.1	0.58 ± 0.04	0.26 ± 0.06
350	2.0 ± 0.1	3.1 ± 0.2	1.9 ± 0.1	0.6 ± 0.07
373	2.3 ± 0.1	2.8 ± 0.2	2.3 ± 0.1	0.7 ± 0.1
400	3.7 ± 0.2	4.8 ± 0.3	4.0 ± 0.2	1.0 ± 0.1
500	8.9 ± 0.4	11 ± 0.9	7.8 ± 0.2	2.2 ± 0.2
647	15 ± 0.5	17 ± 1	13 ± 0.7	5.4 ± 0.3

hydration layer. This interaction mode of the clay particle with the zeolite housing was common across all compositions investigated. The time-dependent topological analysis reveals that the clay forms dynamic, covalent networks with the zeolite housing wall. The covalent bonding is minor, however, and the primary interaction with the housing surface is through the hydration layer. The primary water deficit regions are along the clay–zeolite surface (lower and right sides of the clay particle in Figure 7, top left), opposite to the adherence interface, which is a reliable outcome across the composition series. The housing is slightly oversized (by the clay–zeolite interfaced prepared with 6.5 Å thickness), and during relaxation the particle adheres to one of the walls, leaving a larger gap on the opposing sides.

Table 5. Diffusional Activation Energy E_a for Water and CaOH through Clay–Zeolite Matrix[a]

	E_a (kcal/mol)	D_0 (10^{-7} m^2/s)
clay H_2O	3.4 ± 0.2	2.3 ± 0.6
ZSM-5 H_2O	3.0 ± 0.3	2.0 ± 0.1
CaOH	3.3 ± 0.1	0.7 ± 0.1
QENS data (from ref 43)		
Ca-mont (DSS)	2.3 ± 0.2	1.0 ± 0.2
Ca-mont (DHR)	2.8 ± 0.2	0.6 ± 0.1
bulk H_2O	4.0 ± 0.1	20 ± 4

[a]Also included are QENS data from Sanchez et al.[43] for water and compacted samples for comparsion. DSS and DHR are two fit models used to fit the QENS data[43] and represent systematic error from differing model assumptions.

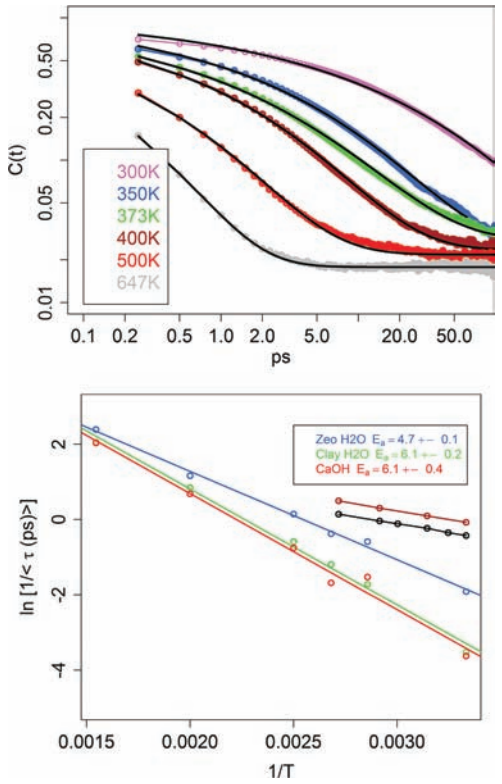

Figure 9. Reorientational dynamics for water. (Top) Stretched exponential fits to the reorientational correlation functions for OH groups in water throughout the clay region. Model fits are shown as black curves for the corresponding temperature. The values are given in Table 6. (Bottom) Arrhenius data for reorientational time versus temperature specifically for water in zeolite (blue) and clay (green and red) regions. Within the clay region, we show OH bound in Ca clusters (red) separately from water (green). The reorientational activation energies are summarized in Table 7 and in the legend (in kcal/mol). The best-fit lines from the present work are shown (blue, green, and red). For comparison, the QENS data from ref 43 are included as with the diffusivity in Figure 8. Lines for the QENS data are visual aids (black and brown).

Given the low level of systemwide hydration (certainly less than the system capacity), water hydrates the clay particle surface selectively around counterions, while dewetting from other regions. The dry regions of the clay particle surface are generally without Ca counterions. Ca was not detected in the zeolite matrix, presumably due to a combination of hydration

dx.doi.org/10.1021/ja208894m | J. Am. Chem. Soc. 2012, 134, 3042–3053

Table 6. Region-Specific Reorientation Times (τ, ps) of Water through the LH0 Model Clay and Silicalite[a]

T (K)	$\langle\tau_{H_2O}^{zeo}\rangle$	$\langle\tau_{H_2O}^{clay}\rangle$	$\langle\tau_{CaOH}^{clay}\rangle$	$\beta_{H_2O}^{zeo}$	$\beta_{H_2O}^{clay}$	β_{CaOH}^{clay}
300	6.7	34	37	0.35	0.36	0.27
350	1.8	5.7	4.6	0.37	0.39	0.32
373	1.5	3.3	5.3	0.34	0.36	0.27
400	0.8	1.8	2.1	0.36	0.40	0.31
500	0.3	0.4	0.5	0.35	0.40	0.34
647	0.09	0.13	0.13	0.40	0.44	0.43

[a]The residual standard error for model fits was less than 3%.

Table 7. Rotational Activation Energy E_a (kcal/mol) for HO Reorientation in the LH0 Model Clay and Silicalite

	$E_a^{H_2O}$
clay H_2O	6.1 ± 0.1
zeolite H_2O	4.7 ± 0.2
$Ca(OH)_2{\cdot}nH_2O$	6.1 ± 0.4

shell size preventing entry to the zeolite and the variety of stabilizing interactions at the clay edges.

A motivation for using the series of model clay compositions was to span a range of layer charge from the highly charged LH0 model to the neutral model LH4, keeping the structure template constant (all models used the same Ca-montmorillonite structural template). We examined the effects of layer charge on basal d spacing, Ca cluster distribution, and diffusivity of water at 300 K.

Figure 7, top left, shows a view of the LH0 smectite particle adhering to the surface of the zeolite housing after the completion of an annealing cycle. The size of the clay particle is on the order of 350 nm^3. The zeolite housing confines the model clay guest particles to an aspect ratio closer to the shape of the zeolite housing unit. Natural smectite particles generally have much larger aspect ratios, which implies the annealed particles in simulation have a higher proportion of edge surface to sheet surface relative to particles in natural samples. We can therefore expect edge interactions to play a stronger role in the model than might be found in natural samples.

The basal spacings in Figure 2 indicate the presence of both bilayer and monolayer hydration patterns, which is in excellent agreement with experiment[7,47] and simulation studies.[16,45] The second Ca layer from the top in Figure 7, top left, is consistent with a monolayer hydration structure. We see that Ca release into the interstitial region is associated with monolayer formation.

Studies of pH dependence on Ca exchange indicate that monolayer hydration in Ca-montmorillonite begins to dominate at low pH, and the transition occurs through the exchange of H_3O^+ for Ca^{2+}. Our final pH across the series reliably acidifies to a range of pH = 1.4−1.8. Ferrage et al.[47] found that bilayer dominates above pH = 2, monolayer hydration proportions in Ca-montmorillonite close to 25% are observed by pH = 1.8, and the proportion rises sharply, leading to monolayer dominance, by pH = 1.4. All Ca compositions in the present series exhibit 25% monolayer hydration and fall in the experimental pH range. Further, the no-Ca control system did not form monolayer hydration but did acidify in the zeolite matrix, suggesting that both Ca and low pH are required for the effect (within our model system).

By contrast, the lack of change in spacings shown in Figure 2 as the layer charge is varied is not what one expects. There are several factors that may contribute to the apparent disconnect between layer charge and basal spacing in the present model. Edge interactions with the zeolite wall, particle adjustments in response to the housing chamber, or hydration interactions with Ca hydrates could all work against the layer charge effects or push the relevant time scale beyond reach of the simulation conditions.

Figure 7 shows closer views of the clay−zeolite housing interface. Two clay sheets (shown in tubes on the left of Figure 7, bottom left) and calcium layers (spheres) are shown interacting with the zeolite wall (tube structure on the right of Figure 7, bottom left and bottom right). Water has diffused away from the initial lattice placement around the clay particle to an equilibrium loading throughout the zeolite matrix and a sparsely hydrated clay surface. Hydration of the clay surface is primarily at the adherence interface of the clay particle and the zeolite wall, which leaves dry patches of the clay surface opposite the adherence interface. Silanols uniformly coat the surface of both the zeolite and the clay edges, regardless of the post-annealing hydration distribution, indicating that silanol formation was complete prior to equilibrium distribution of water.

Silanol groups that emerged reactively are visible on both zeolite and clay surfaces and can be seen throughout the images in Figure 7. O_nAl−OH species are present in trace amounts on the clay edge. The surface adsorption of OH^- and release of H^+ resulted in acidification of the system, as shown in Figure 6. $[H^+](t)$ exceeds the initial increase of $[HO^-](t)$ from lime hydrate formation and ultimately acidifies the system.

Chemical isolation of the LHHs in simulation was important to verify, as it was a model assumption utilized in the series definition. Chemical isolation is consistent with thermal degradation studies of montmorillonite, which show that the LHHs are thermally tenacious and liberate at temperatures exceeding those studied here (>900 K), with the consequent irreversible degradation of the clay lattice.[46] It is perhaps more surprising that, in the case of LH0, the vacant LHH sites are fully insulated from solvent (in simulation) and show no tendency to take up protons. Within the context of the model clays, the silicate structure is an effective kinetic barrier to proton migration. For the present work, the use of differing LHH patterns to study layer charge is therefore valid.

The Ca cluster distribution shows in the case of LH3 that the use of the initial counterion $CaOH^+$ led to increased Ca precipitation in the interlayer. We should note that the initial arrangement of $CaOH^+$ as individual molecules is lost within the first few picoseconds, and $Ca(OH)_2{\cdot}nH_2O$ equilibria evolves in the confined interlayer regions, with the endowed hydration and hydration flux occurring at the edges. The main factor responsible for precipitate formation appears to be a lower H/O ratio near Ca in the interlayer relative to the other compositions.

The sensitivity of Ca precipitate cluster size in the interlayer is also consistent with the pH dependence of $Ca(OH)_2$ solubility and Ca exchange.[47] The range of $Ca(OH)_2{\cdot}nH_2O$ structures is dynamic and complex (see cluster size distribution in Figure 3). The extent of transient cluster formation is sensitive to the bonding threshold. At 300 K and $\Theta_{min} > 0.4$, clusters in LH4, LH2, and LH0 contained 1−4 Ca ions with varying degrees of hydration and protonation. As can be seen in Figure 7, the OH orientation in the calcium environment is fairly ordered, with OH^-, H_2O, or H_3O^+ OH bond vectors oriented from the Ca to the clay surface in the case of the

dx.doi.org/10.1021/ja208894m | J. Am. Chem. Soc. 2012, 134, 3042−3053

hydration bilayer (top and lower two calcium layers in Figure 7, top left). In the case of monohydration (second calcium layer from the top in Figure 7, top left), the OH favors in-plane orientation rather than perpendicular to the clay sheets. In the LH3 system, we see a qualitative difference in the morphology of the Ca clusters in the monolayer vs bilayer interlayer hydration. In models with the smaller Ca clusters (LH0, LH2, LH4), the bilayer hydration gives a clumpier distibution of Ca clusters as opposed to a more chain-like morphology in the case of the monolayer. With the LH3 system, the same trend is amplified, and a similar distinction of large clumps in the bilayer hydration vs longer chains in the monolayer hydration emerges. If the distinction between monolayer and bilayer hydration is pH sensitive, as is found experiementally,[47] then one could argue that the microscopic details of H_3O^+-driven exchange of Ca^{2+} may more directly involve a complex response of interlayer $Ca(OH)_2{\cdot}nH_2O$ to changes in both pH and humidity. This would be entirely consistent with experimental results for both low pH[47] and low humidity.[7] A more focused study along these lines may well inform further mechanistic details of pH-driven Ca exchange in Ca-montmorillonite. Insights we can offer here are the following: (a) interlayer Ca clusters form under our model conditions; (b) the clusters have a distinct morphology in monolayer vs bilayer hydration patterns; (c) both are sensitive to pH and humidity; and (d) interlayer Ca clusters in monolayer and bilayer hydration patterns may have distinct pH profiles.

Diffusion and rotational relaxation in montmorillonite clays with varying counterions have been reported in simulation[18,48] and experimental[42,43,49] groups. Results generally agree on orders of magnitude, but differences in experimental techniques, methods of analyses, and simulation conditions present a myriad of considerations when attempting insightful comparisons.[18,43,49,50] In contrast, transport properties of zeolites in the context of a range of solutes have been extensively studied (see ref 51 for a review).

To characterize the dynamics of water in the clay vs the zeolite matrix, we collected statistics for each region and applied the method of Liu and Berne[41] for treating diffusion through regions. We calculated regional-specific Arrhenius parameters for diffusion over a wide temperature range. The resulting values for both clay and zeolite regions independently compare well to available measures and simulations of the pure environments. The ReaxFF method allowed further examination within the clay region of the impact Ca hydrate complexation has on water dynamics.

Figure 4 shows the diffusivity of water at 300 K in comparison to corresponding QENS measurements where possible. There is an apparent but weak trend of increased water diffusivity in the zeolite with decreased charge on the clay; that is, water mobility is highest in the zeolite matrix with the neutral pyrophyllite model particle without Ca salts. Adding Ca and increasing layer charge decreases water diffusivity in the zeolite (Figure 4, blue series). Water diffusivity in the clay region lacks a clear dependence on layer charge (Figure 4, red series). Diffusivity of water in the clay region is highest at the two opposing extremes of LH0 and LH4W. For the highly charged LH0, the annealing procedure slightly increased diffusivity at 300 K (compare post-annealed $D^{clay}_{H_2O} = 0.8 \times 10^{-9}$ m^2/s to reference value for the annealing control run $D^{clay}_{H_2O} = 0.6 \times 10^{-9}$ m^2/s at 300 K). Experimentally, the Ca-illite mica has higher diffusivity than the Ca-montmorillonite sample. The pyrophyllite model LH4W has a bilayer hydration pattern in each interlayer, which is more comparable to an exfoliated form. It is plausible to suspect its stability is due to surface interactions with the zeolite housing.

Figure 8, bottom, compares our calculated Arrhenius parameters to QENS measurements of compacted Ca-montmorillonite samples taken from Sánchez et al.[43] Bulk water (brown) and fully hydrated Ca-montmorillonite particles that were fit with two different analysis models (shown in black and gray) are shown for reference. The compacted samples were fully hydrated, which gives a bilayer hydration pattern. We expect water mobility to be slower under the simulated levels of hydration. However, mesoporous crevices between clay particles in the samples permit water flow that may approach bulk-like rates as the interlayer crevice increases in size. The observation that the samples show reduced mobility relative to bulk water indicates that confining effects operate, but it is unclear what relative effects these crevices have versus the interlayer and surface water. Again, we expect clay edge effects to play a stronger role in the present scheme than we would find in natural samples with much larger aspect ratios.

Diffusivity for water in the clay particle region ($D^{clay}_{H_2O} = 5.8 \times 10^{-10}$ m^2/s) at 300 K is about a quarter of the QENS bulk water value of 2.3×10^{-9} m^2/s and compares well to the measured diffusivities of fully hydrated compacted samples[43] of Ca-montmorillonite of 9×10^{-10} and 12×10^{-10} m^2/s. The same work reported values for half-hydrated Ca-montmorillonite of 4.6×10^{-10} and 4.1×10^{-10} at 298 K, depending on the choice of fitting model used (open black and gray circles in Figure 8, bottom). Considering the range of systematic error introduced by different fitting models, our regional specific diffusion of water around the clay particle and within the interlayers is in good agreement with their Ca-montmorillonite measurements.

The calculation of $D^{clay}_{H_2O}$ selected only water within the clay region that was not complexed with Ca hydrates. The slower diffusing Ca hydrate groups would, however, be included in experimental measurements. We treated the mobility of HO··· groups bound to calcium hydrate clusters separately as D^{clay}_{CaOH}. Values are given in Table 4 and shown in red in Figure 8, bottom. The specific inclusion criterion for this class is that a given H is connected to an oxygen in a cluster (defined with $\Theta_{min} > 0.4$) containing at least one calcium and no silicon (hydrates of Ca counterions).

Our calculated silicalite water diffusion coefficient at the time of annealing onset ($D^{clay}_{H_2O}$) at 300 K of 1.2×10^{-9} m^2/s compares well to previously reported PFG NMR measurements[44] of 1.7×10^{-9} m^2/s for silicalite (magenta open circle in Figure 8, bottom). This is an improvement over the simulated results of 3.3×10^{-9} m^2/s reported from use of classical MD potentials parametrized for silicalite.[44] Annealing, however, reduced the diffusivity of the zeolite (see Figure 4, blue series). Figure 6 shows that the main difference in the zeolite is acidification. The present results suggest that the reason for the systematic reduction of zeolite water diffusivity after annealing is that the presence of hydronium ion slows the diffusivity of water.

The diffusivity of OH bound to Ca is less than half that of the water throughout the clay particle ($D^{clay}_{CaOH}/D^{clay}_{H_2O} \approx 0.45$). This difference holds well across a wide range of temperatures, as reflected by the similar activation energies for diffusion of OH in the two differing chemical environments. The

dx.doi.org/10.1021/ja208894m | J. Am. Chem. Soc. 2012, 134, 3042−3053

differences in this case are therefore well characterized by differences in the Arrhenius frequency or pre-exponential factors for the two processes.

We should emphasize that the model diffusion coefficients were calculated from diffusion in the specific environment shown in Figure 1, and the variety of interactions present may not represent the variety found in different physical samples. It is noteworthy that diffusion in the present simulation of the clay−zeolite composite environment agrees well with both PFG NMR and QENS measurements of the corresponding pure materials, particularly since the two experimental techniques measure these rates on very different length and time scales. The present level of agreement with experiment is encouraging for the prospect of further improving accuracy by including more physical sample-specific aspects in the model system.

The diffusive E_a from QENS data for water in hydrated Ca-montmorillonite samples is lower than for bulk water (2.8 kcal/mol for clay samples vs 4 kcal/mol for bulk water[43]). A value of E_a = 4 kcal/mol for bulk water reflects the strength of the H-bonds that break and reform through diffusive processes. A smaller temperature dependence in the clay samples suggests the H-bonds between water and the clay surface are weaker than in bulk. Sánchez et al. suggested that competition between cations and the clay surface may distort the H-bonds and could reduce E_a. They note that the jump lengths in montmorillonite are significantly longer than in bulk water, implying weaker H-bonds.[43] A similar interpretation was offered in a recent study of nanoconfined water in phyllosilicates,[52] where the authors suggested that the disruption of hydrogen-bonding paterns in water by librational distortions of the silicate tetrahedra lowers the energy barrier to diffusion. We also see lower activation for diffusion relative to bulk (E_a = 3 and 3.4 kcal/mol for water in zeolite and clay regions, respectively; Table 5).

Our calculated reorientation rates for water are slower than the QENS data at T = 298 K (also reported in Sanchez et al.[43]) and have a stronger temperature dependence, as shown in Figure 9, bottom. The QENS data for rotational relaxation show similar rates for water in bulk and Ca-montmorillonite samples, with essentially the same temperature dependence. However, data from the same experiments showed distinct temperature dependencies for diffusion. The authors suggested the possibility that bulk-like water between crevices might dominate rotational relaxation.[43]

The interpretation of reorientational rates in water has a controversial history.[10,50,53] Water in confined environments behaves differently than in bulk.[54] We expect the effects of confinement to slow the reorientation rates. We further expect a coupling between rotation and translation.[50]

Examining the values of the stretched exponential factor β in Table 6 suggests that our calculated average rotational rates are well described by a broad distribution of rotational lifetimes, which is also expected for water in complex surface environments.[42,49,54]

Our calculated rotational rates for water in the clay environment and OH bound to Ca complexes show essentially the same temperature dependence and rotational rate across the full temperature range investigated. The absolute diffusion rates were quite different when water was complexed to Ca, but the difference is well described solely by the differences in the Arrhenius pre-exponential factor for diffusion. A consistent activation energy for both diffusion and rotational processes supports a consistent mechanism for diffusion and rotation for water diffusing through the clay environment versus water diffusing while complexed to Ca in the clay interlayers.

Insights from the present simulations suggest that a possible explanation for the diffusive difference of CaOH versus water might be related to transient cluster formation of Ca-$(OH)_2{\cdot}nH_2O$ in the planar confinement of the clay interlayers. It is plausible to suggest that Ca hydrate clusters larger than the interlayer spacing may have correlated diffusive modes in the confining plane of the interlayer. The mechanisms of translation and rotation across the clay surface may still show a similar temperature dependence, but the absolute rates of diffusion may be slowed in the case of transient hydrate clusters. Net displacements of transient hydrate clusters result when there is a collective diffusive motion of the water within the hydrate clusters. This effect would reduce the probability of water displacement but not necessarily require a change in mechanism, and could explain a difference in the diffusive pre-exponential factors with consistent activation energies.

■ CONCLUSION

We find that the reactive annealing approach taken here provides an effective means of preparing large-scale clay−zeolite composite systems for studying the structure and dynamics of transport processes in clay−zeolite composites. The approach offers a practical means of preparing freely diffusing (nonperiodic) nanometer-scale clay particles in a periodic zeolite matrix under conditions of dynamic chemical equilibrium. Hydration of the clay interlayers, silanol formation on exposed surfaces, and overall geometry compare well to available experimental data. The regional-specific dynamics of water diffusing through the clay−zeolite composite also compares well to available experimental measures in the analogous pure systems. The acid/base equilibria showed reasonable values for pH of the $Ca(OH)_2{\cdot}nH_2O$ environment and silanol formation process.

The construction protocol described produces smectite models where a mixed monolayer and bilayer hydration emerges within the simulation. There many open questions regarding the atomistic details of hydration transitions in swelling clays. The present approach provides a practical means of addressing these questions in a fully explicit reactive context.

We find that diffusion of water when complexed to Ca hydrates is considerably slower than freely diffusing water over the clay surface. More specifically, the reduction in mobility is well described by a difference in the Arrhenius pre-exponential factor, rather than a change in activation energy that would affect the temperature dependence. We suggest that transient Ca hydrate clusters reduce the net probability of displacement relative to freely diffusing water, but that once displacement of a transient cluster occurs, it occurs with a similar underlying mechanism of breaking and forming new H-bonds, and therefore has a temperature dependence similar to that of uncomplexed water mobility across the clay surface.

Finally, it is worth commenting that the present approach is applicable to a wider range of particles placed in the housing region utilizing a similar periodic zeolite shell scheme. This is particularly encouraging for further investigations of a broader range of solutes where dynamic chemical equilibrium complicates the application of empirical force fields. Further investigation into differing salt effects and cluster formation is warranted, as well as a more detailed investigation of the hydration transitions exhibited by the present model smectite particles.

AUTHOR INFORMATION

Corresponding Author
pitman@us.ibm.com

ACKNOWLEDGMENTS

The authors thank Ruhong Zhou and Bruce J. Berne for helpful comments and contributions to the dynamics analysis, and Payel Das for helpful discussions and comments on the manuscript. This work was supported by the Computational Biology Center at IBM–Thomas J. Watson Research Center. ACTvD's work was sponsored by the Division of Chemical Sciences, Geosciences and Biosciences, Office of Basic Energy Sciences, U.S. Department of Energy.

REFERENCES

(1) Swadling, J. B.; Coveney, P. V.; Greenwell, H. C. *J. Am. Chem. Soc.* **2010**, *132*, 13750–13764.
(2) Smith, J. V.; Frederick, P.; Arnold, J.; Parsons, I.; Lee, M. R. *Proc. Natl. Acad. Sci. U.S.A.* **1999**, *96*, 3479–3485.
(3) Hughes, Z. E.; Carrington, L. A.; Raiteri, P.; Gale, J. D. *J. Phys. Chem. C* **2011**, *115*, 4063–4075.
(4) Gimmi, T.; Kosakowski, G. *Environ. Sci. Technol.* **2011**, *45*, 1443–1449.
(5) Greathouse, J. A.; Cygan, R. T. *Environ. Sci. Technol.* **2006**, *40*, 3865–3871.
(6) Churakov, S. V.; Gimmi, T. *J. Phys. Chem. C* **2011**, *115*, 6703–6714.
(7) Paineau, E.; Bihannic, I.; Baravian, C.; Philippe, A.-M.; Davidson, P.; Levitz, P.; Funari, S. S.; Rochas, C.; Michot, L. J. *Langmuir* **2011**, *27*, 5562–5573.
(8) Paineau, E.; Michot, L. J.; Bihannic, I.; Baravian, C. *Langmuir* **2011**, *27*, 7806–7819.
(9) Smith, D. E.; Wang, Y.; Chaturvedi, A.; Whitley, H. D. *J. Phys. Chem. B* **2006**, *110*, 20046–20054.
(10) Laage, D.; Hynes, J. T. *Science* **2006**, *311*, 832–835.
(11) Suter, J. L.; Coveney, P. V.; Greenwell, H. C.; Thyveetil, M. A. *J. Phys. Chem. C* **2007**, *111*, 8248–8259.
(12) Mazo, M. A.; Manevitch, L. I.; Gusarova, E. B.; Shamaev, M. Y.; Berlin, A. A.; Balabaev, N. K.; Rutledge, G. C. *J. Phys. Chem. B* **2008**, *112*, 2964–2969.
(13) Ferrage, E.; Sakharov, B. A.; Michot, L. J.; Delville, A.; Bauer, A.; Lanson, B.; Grangeon, S.; Frapper, G.; Jiménez-Ruiz, M.; Cuello, G. J. *J. Phys. Chem. C* **2011**, *115*, 1867–1881.
(14) Botan, A.; Rotenberg, B.; Marry, V.; Turq, P.; Noetinger, B. *J. Phys. Chem. C* **2010**, *114*, 14962–14969.
(15) Aristilde, L.; Marichal, C.; Miéhé-Brendlé, J.; Lanson, B.; Charlet, L. *Environ. Sci. Technol.* **2010**, *44*, 7839–7845.
(16) Yu, Y.; Yang, X. *Phys. Chem. Chem. Phys.* **2011**, *13*, 282–290.
(17) Scocchi, G.; Posocco, P.; Fermeglia, M.; Pricl, S. *J. Phys. Chem. B* **2007**, *111*, 2143–2151.
(18) Demontis, P.; Gulín-González, J.; Jobic, H.; Suffritti, G. B. *J. Phys. Chem. C* **2010**, *114*, 18612–18621.
(19) Cygan, R. T.; Liang, J.-J.; Kalinichev, A. G. *J. Phys. Chem. B* **2004**, *108*, 1255–1266.
(20) Voora, V. K.; Al-Saidi, W. A.; Jordan, K. D. *J. Phys. Chem. A* **2011**, *115*, 9695–9703.
(21) Larentzos, J. P.; Greathouse, J. A.; Cygan, R. T. *J. Phys. Chem. C* **2007**, *111*, 12752–12759.
(22) Salles, F.; Bildstein, O.; Douillard, J. M.; Jullien, M.; Raynal, J.; Van Damme, H. *Langmuir* **2010**, *26*, 5028–5037.
(23) Salles, F.; Devautour-Vinot, S.; Bildstein, O.; Jullien, M.; Maurin, G.; Giuntini, J.-C.; Douillard, J.-M.; Damme, H. V. *J. Phys. Chem. C* **2008**, *112*, 14001–14009.
(24) van Duin, A. C. T.; Dasgupta, S.; Lorant, F.; Goddard, W. A. III *J. Phys. Chem. A* **2001**, *105*, 9396–9409.
(25) Zybin, S. V.; Goddard, W. A. III; Xu, P.; van Duin, A. C. T.; Thompson, A. P. *Appl. Phys. Lett.* **2010**, *96*, 081918.
(26) Brenner, D. W. *Phys. Rev. B* **1990**, *42*, 9458–9471.
(27) Tersoff, J. *Phys. Rev. Lett.* **1988**, *61*, 2879–2882.
(28) Abell, G. C. *Phys. Rev. B* **1985**, *31*, 6184–6196.
(29) Pauling, L. *J. Am. Chem. Soc.* **1947**, *69*, 542–553.
(30) Mortier, W. J.; Ghosh, S. K.; Shankar, S. *J. Am. Chem. Soc.* **1986**, *108*, 4315–4320.
(31) Viani, A.; Gualtieri, A. F.; Artioli, G. *Am. Mineral.* **2002**, *87*, 966–975.
(32) Plimpton, S. *J. Comp. Phys.* **1995**, *117*, 1–19.
(33) Raymand, D.; van Duin, A. C.; Goddard, W. A. III; Hermansson, K.; Spångberg, D. *J. Phys. Chem. C* **2011**, *115*, 8573–8579.
(34) Raymand, D.; van Duin, A. C.; Spångberg, D.; Goddard, W. A. III; Hermansson, K. *Surf. Sci.* **2010**, *604*, 741–752.
(35) Aryanpour, M.; van Duin, A. C. T.; Kubicki, J. D. *J. Phys. Chem. A* **2010**, *114*, 6298–6307.
(36) Fogarty, J. C.; Aktulga, H. M.; Grama, A. Y.; van Duin, A. C. T.; Pandit, S. A. *J. Chem. Phys.* **2010**, *132*, 174704.
(37) van Duin, A. C. T.; Bryantsev, V. S.; Diallo, M. S.; Goddard, W. A. III; Rahaman, O.; Doren, D. J.; Raymand, D.; Hermansson, K. *J. Phys. Chem. A* **2010**, *114*, 9507–9514.
(38) Russo, M. F. Jr.; Li, R.; Mench, M.; van Duin, A. C. T. *Int. J. Hydrogen Energy* **2011**, *36*, 5828–5835.
(39) Manzano, H.; Meoeini, S.; van Duin, A. C. T.; Marinelli, F.; Ulm, F.-J.; Pellenq, R. Manuscript in preparation, 2011.
(40) Russo, M. F.; van Duin, A. C. T. *Nucl. Instrum. Methods Phys. Res. Sect. B* **2011**, *269*, 1549–1554.
(41) Liu, P.; Harder, E.; Berne, B. J. *J. Phys. Chem. B* **2004**, *108*, 6595–6602.
(42) Swenson, J.; Bergman, R.; Longeville, S. *J. Chem. Phys.* **2001**, *115*, 11299.
(43) Sánchez, F. G.; Jurányi, F.; Gimmi, T.; Loon, L. V.; Unruh, T.; Diamond, L. W. *J. Chem. Phys.* **2008**, *129*, 174706.
(44) Bussai, C.; Hannongbua, S.; Fritzsche, S.; Haberlandt, R.; R Aiello, G. G.; Testa, F. *Stud. Surf. Sci. Catal.* **2002**, *142*, 1979–1986.
(45) Ferrage, E.; Sakharov, B. A.; Michot, L. J.; Delville, A.; Bauer, A.; Lanson, B.; Grangeon, S.; Frapper, G.; Jimenez-Ruiz, M.; Cuello, G. J. *J. Phys. Chem. C* **2011**, *115*, 1867–1881.
(46) Farmer, V. C.; Russell, J. Infrared Absorption Spectroscopy in Clay Studies. Fifteenth Conference on Clays and Clay Minerals, 1967; http://www.clays.org/journal/archive/volume%2015/15-1-121.pdf.
(47) Ferrage, E.; Tournassat, C.; Rinnert, E.; Lanson, B. *Geochim. Cosmochim. Acta* **2005**, *69*, 2797–2812.
(48) Marry, V.; Turq, P.; Cartailler, T.; Levesque, D. *J. Chem. Phys.* **2002**, *117*, 3454.
(49) Swenson, J.; Bergman, R.; Howells, W. S. *J. Chem. Phys.* **2000**, *113*, 2873.
(50) Stirnemann, G.; Sterpone, F.; Laage, D. *J. Phys. Chem. B* **2011**, *8*, 3254–3262.
(51) Bowen, T. C.; Noble, R. D.; Falconer, J. L. *J. Membr. Sci.* **2004**, *245*, 1–33.
(52) Ockwig, N. W.; Greathouse, J. A.; Durkin, J. S.; Cygan, R. T.; Daemen, L. L.; Nenoff, T. M. *J. Am. Chem. Soc.* **2009**, *131*, 8155–8162.
(53) Nienhuys, H.-K.; van Santen, R. A.; Bakker, H. J. *J. Chem. Phys.* **2000**, *112*, 8487.
(54) Brovchenko, I.; Oleinkova, A. *Interfacial and Confined Water*; Elsevier: Amsterdam, 2008.